

Effects of Atmospheric Aging Processes on Nascent Sea Spray Aerosol Physicochemical Properties

Chathuri P. Kaluarachchi, Victor W. Or, Yiling Lan, Elias S. Hasenecz, Deborah Kim, Chamika K. Madawala, Glorianne Dorcé, Kathryn J. Mayer, Jonathan S. Sauer, Christopher Lee, Christopher D. Cappa, Timothy H. Bertram, Elizabeth A. Stone, Kimberly A. Prather, Vicki H. Grassian, and Alexei V. Tivanski*



Cite This: <https://doi.org/10.1021/acsearthspacechem.2c00258>



Read Online

ACCESS |

Metrics & More

Article Recommendations

ABSTRACT: The effects of atmospheric aging on single-particle nascent sea spray aerosol (nSSA) physicochemical properties, such as morphology, composition, phase state, and water uptake, are important to understanding their impacts on the Earth's climate. The present study investigates these properties by focusing on the aged SSA (size range of 0.1–0.6 μm) and comparing with a similar size range nSSA, both generated at a peak of a phytoplankton bloom during a mesocosm study. The aged SSAs were generated by exposing nSSA to OH radicals with exposures equivalent to 4–5 days of atmospheric aging. Complementary filter-based thermal optical analysis, atomic force microscopy (AFM), and AFM photothermal infrared spectroscopy were utilized. Both nSSA and aged SSA showed an increase in the organic mass fraction with decreasing particle sizes. In addition, aging results in a further increase of the organic mass fraction, which can be attributed to new particle formation and oxidation of volatile organic compounds followed by condensation on pre-existing particles. The results are consistent with single-particle measurements that showed a relative increase in the abundance of aged SSA core–shells with significantly higher organic coating thickness, relative to nSSA. Increased hygroscopicity was observed for aged SSA core–shells, which had more oxygenated organic species. Rounded nSSA and aged SSA had similar hygroscopicity and no apparent changes in the composition. The observed changes in aged SSA physicochemical properties showed a significant size-dependence and particle-to-particle variability. Overall, results showed that the atmospheric aging can significantly influence the nSSA physicochemical properties, thus altering the SSA effects on the climate.

KEYWORDS: atomic force microscopy, aged sea spray aerosol, morphology, phase state, water uptake, composition, particle-to-particle variability

INTRODUCTION

Nascent sea spray aerosols (nSSA) are generated upon the bursting of air bubbles at the ocean–air interface and represent a significant fraction of natural aerosol mass concentration in the atmosphere.^{1–4} During air bubble bursting, organic, inorganic, and biological species from the seawater and sea surface microlayer (SML) can be transferred into the nSSA.^{1,3–15} Therefore, the chemical complexity of nSSA can significantly vary due to the composition and biological activity in the seawater and SML.^{3,4,14–23} Additionally, the differences in formation mechanisms (i.e., film drops vs jet drops) of nSSA at the ocean–air interface can further control their size-dependent and particle-to-particle variability in chemical complexity.^{5,14,16,24} nSSA can influence the Earth's radiative budget directly, via scattering and absorbing incoming solar radiation, and indirectly by acting as cloud condensation nuclei (CCN) or ice nuclei (IN).^{1,6,7,13,25–35} The surfaces of aerosols can facilitate atmospheric aging with gaseous phase oxidants (i.e., OH radicals and ozone).^{36–44} For example, studies conducted on atmospherically relevant organic model systems

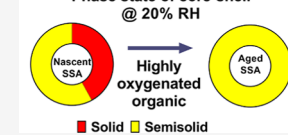
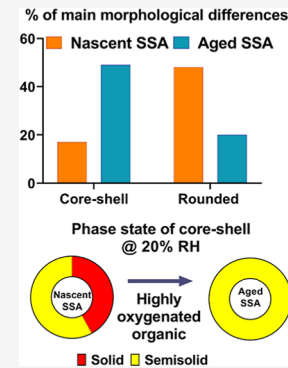
showed that atmospheric aging can lead to the formation of new particles,^{2,45} oxidation of volatile and semi-volatile organic compounds from pre-existing particles,^{36–38,46–48} and condensation of oxidized organics on pre-existing particles to form coatings.^{36,46–49} Thus, atmospheric aging can alter the nSSA's physicochemical properties (i.e., morphology, composition, phase states, and water uptake) and influence on their direct and indirect aerosol effects on the climate.^{36–38,46,50}

The effects of aging on the physicochemical properties of aerosols have been studied previously using laboratory-generated model systems. For example, atmospheric organic aerosol proxies (e.g., alkanes and oxidized organic compounds)

Received: August 18, 2022

Revised: September 30, 2022

Accepted: October 6, 2022



58 showed a formation of highly oxygenated organic compounds
59 with increasing atmospheric aging time (i.e., increasing OH
60 exposure).^{36,47,48,51} The morphology of aerosols can have a
61 significant impact on the rates of atmospheric aging.³⁶ In
62 particular, core–shells can undergo the OH-initiated aging
63 process within days, compared to rounded particles where the
64 timescale can be weeks or even months.^{36,52} In addition, an
65 increase in hygroscopicity and water uptake efficiency of
66 aerosols have been observed due to the atmospheric aging,
67 which in turn impacts their phase state.^{36,43,47,53,54} The
68 changes in the phase state can change aerosol's water content,
69 solute concentration, and viscosity that subsequently alter their
70 direct and indirect effects.^{1,2,11,42,55–58} However, to our
71 knowledge, no previous studies had investigated the effects
72 of atmospheric aging on physicochemical properties of single-
73 particle nSSA and their size-dependent particle-to-particle
74 variabilities.

75 Herein, we investigated the effects of atmospheric aging on
76 various physicochemical properties of nSSA (size range of 0.1–
77 0.6 μm) generated during a phytoplankton bloom from the Sea
78 Spray Chemistry And Particle Evolution (SeaSCAPE)
79 mesocosm study in 2019.^{1,2} Aged SSAs were generated by
80 exposing freshly generated nSSA to OH radicals, simulating
81 approximately 4–5 days of atmospheric aging. In addition, the
82 formation of new particles (i.e., secondary marine aerosols)
83 and condensation of oxidized organic compounds on existing
84 particles were observed. Filter-based thermal optical analyses
85 and ion chromatography were used to investigate the size-
86 dependent bulk-ensemble organic mass fraction in nSSA and
87 aged SSA, which provided ensemble-averaged composition
88 data for the aerosol population, with significant organic
89 enrichment observed for aged SSA. To better understand the
90 particle-to-particle variability in nSSA versus aged SSA organic
91 enrichment and their corresponding morphology, phase state,
92 and water uptake properties, single-particle atomic force
93 microscopy (AFM) and AFM–photothermal infrared spec-
94 troscopy (AFM–PTIR) analyses were employed. A significant
95 change of these properties was observed due to the
96 atmospheric aging, and results provide an important insight
97 on how the aging influences the physicochemical properties of
98 nSSA.

99 ■ MATERIALS AND METHODS

100 **Nascent and Aged SSA Generation and Collection for**
101 **Offline Single-Particle Studies.** Nascent SSA (nSSA) were
102 generated throughout a phytoplankton bloom from a wave-
103 simulation channel facility which contained filtered seawater
104 from the southern coast of California, during the Sea Spray
105 Chemistry And Particle Evolution (SeaSCAPE) 2019 study.^{1,2}
106 A micro-orifice uniform deposit impactor (MOUDI; MSP,
107 Inc., model 110) at a flow rate of 30 L/min was used to deposit
108 individual submicrometer nSSA onto hydrophobically coated
109 (Rain-X) silicon substrates (Ted Pella, Inc.) at ~80% relative
110 humidity (RH).¹ The MOUDI stages 7, 8, and 9 were used
111 that correspond to 50% cutoff aerodynamic diameter range of
112 0.32–0.60, 0.18–0.32, and 0.10–0.18 μm , respectively.
113 Additional details of the nSSA generation and deposition can
114 be found elsewhere.¹ For the purpose of comparison, both
115 nSSA and aged SSA were collected on the same sampling day
116 (peak of the bloom, August 2nd) over the same size range.
117 A potential aerosol mass oxidation flow reactor (PAM-OFR,
118 Aerodyne Inc) was used to produce hydroxyl (OH) radicals,
119 which can simulate aging of aerosols with atmospheric time-

120 equivalent aging from a fraction of a day to several weeks.^{2,59,60}
121 Here, by using the PAM-OFR, aged SSA were generated by
122 exposing nSSA to OH radicals (average concentration of \sim 5.9
123 $\times 10^{11}$ molecules/cm³, aerosol residence time of \sim 2 min),
124 which corresponds to 4–5 days of atmospheric aging.^{2,59}
125 Before aging, nSSA stream was passed through a denuder
126 (CARULITE-200, Ozone Solutions) to remove ozone (O₃)
127 from the wave-channel headspace.² Additional details of the
128 aged SSA generation using the PAM-OFR can be found
129 elsewhere.² The PAM-OFR sampled nSSA from a headspace of
130 the wave-channel to generate aged SSA.^{1,2} However, in
131 addition to aged SSA, new particle formation (i.e., secondary
132 marine aerosols, SMA, typical particle diameter < 100 nm) was
133 also observed, likely as a result of oxidation and condensation
134 of volatile organic compounds from the wave-channel
135 headspace.² In the present work, atomic force microscopy
136 (AFM) single-particle analysis was limited to particle sizes
137 above 100 nm, thus largely excluding SMA particles that were
138 < 100 nm in size. In addition, we note that the composition of
139 aged SSA studied here may be somewhat influenced by
140 condensation of oxidized volatile or semi-volatile organic
141 compounds onto pre-existing particles in PAM-OFR. The
142 generated aged SSA were deposited onto hydrophobically
143 coated silicon substrates using MOUDI (MSP, Inc., model
144 125R, flow rate 10 L/m) stages of 7, 8, and 9 at \sim 20% RH. All
145 samples were stored in clean Petri dishes and kept inside a
146 laminar flow hood (NuAire, Inc., NU-425-400) at ambient
147 temperature (20–25 °C), 20–25% relative humidity range,
148 and pressure for 2–4 months prior to AFM and AFM–PTIR
149 experiments.

150 **AFM Imaging to Determine the Morphologies and**
151 **Organic Volume Fraction of Aged SSA Core–Shell at**
152 **20% RH.** Particle locations for single-particle imaging and
153 analysis were selected in a completely random and unbiased
154 manner.¹ A molecular force probe 3D AFM (Asylum Research,
155 Santa Barbara, CA) was used for imaging individual substrate-
156 deposited aged SSA at ambient temperature (20–25 °C) as
157 described in prior studies.^{1,11,55,61} A custom-made humidity
158 cell was used to control RH with a range of 20–80%.¹¹ Prior to
159 the AFM measurements at a particular RH, at least 10 min of
160 equilibrium time was allocated to ensure that aged SSA are in
161 thermodynamic equilibrium with surrounding water
162 vapor.^{11,55,61} Silicon nitride AFM tips (MikroMasch, model
163 CSC37, typical tip radius of curvature of \sim 10 nm, nominal
164 spring constant of 0.5–0.9 N/m) were used for imaging and
165 force spectroscopy measurements.^{11,55,61} AFM AC (intermit-
166 tent contact) mode imaging was used to collect 3D height and
167 phase images of individual aged SSAs to determine their
168 morphology and volume-equivalent diameter and quantify the
169 organic volume fraction (OVF) and corresponding organic
170 coating thickness (OCT) for core–shell aged SSA, as
171 described in prior studies.^{11,55,61} The OVF is defined as the
172 ratio of the shell volume (assumed predominantly organic) to
173 the total particle volume, while the OCT represents the
174 projected thickness of organic coating around the inorganic
175 core.^{1,11,61,62} By assuming the core is predominantly inorganic
176 and the shell primarily organic, the single-particle OVF
177 represents the amount of organic present in the particle
178 relative to the total particle volume.^{1,11,61} For the morpho-
179 logical analysis, approximately 100 individual aged SSAs were
180 investigated, while for the OVF and OCT analyses, 10 or more
181 individual aged SSA core–shell within each size range were
182 investigated. The relative abundance of identified morpho-

183 logical categories (rounded, core–shell, prism-like, rod–shell, 184 and aggregate) and OVF and OCT values were recorded as an 185 average and one standard deviation at three volume-equivalent 186 diameter ranges of 0.10–0.18, 0.18–0.32, and 0.32–0.60 μm . 187 The observed aged SSA morphology, OVF, and OCT were 188 compared with nSSA sample collected on same sampling day 189 over the same three size ranges.¹

190 Because the total number of individual particles that can be 191 practically studied with AFM is limited, we utilized a statistical 192 probability distribution analysis to assess the statistical 193 significance of the AFM-based morphology and phase state 194 measurements.¹ The detailed description about the approach 195 can be found elsewhere.^{1,63,64} Briefly, the probability 196 distributions associated with the likelihood of sampling one 197 of the five morphologies, or one of the three phase states, were 198 generated using a self-coded Monte Carlo-like simulation 199 method for a “true” population of 10,000 particles.^{1,63–65} The 200 average with one standard deviation for the fraction of particles 201 from each morphological type or phase states were obtained by 202 fitting the probability distribution plots with the Gaussian 203 function.¹ The results were recorded for nSSA and aged SSA 204 samples as a function of RH and volume-equivalent diameter 205 range.

206 **AFM Measurements of Aged SSA Water Uptake and 207 Phase State at RH Range of 20–80%.** The analysis of 3D 208 growth factor (GF) at 80% RH was employed to quantify the 209 water uptake properties of aged SSA on a single-particle 210 basis.^{1,66–68} The GF is defined as the ratio of the volume- 211 equivalent diameter of an individual SSA at 80% RH over the 212 corresponding volume-equivalent diameter recorded at 20% 213 RH, where higher values would indicate the presence of more 214 hygroscopic components.^{1,66–68} The GF measurements were 215 performed on approximately 10 individual core–shell and 216 rounded aged SSA at their highest relative occurrence size 217 range of 0.32–0.60 and 0.10–0.18 μm , respectively, and the 218 values were reported as an average and one standard deviation.

219 The AFM force spectroscopy was employed to identify the 220 phase state at 20 and 60% RH under ambient temperature 221 (20–25 °C) and pressure for aged SSA with the most 222 abundant morphologies (i.e., core–shell, rounded) using a 223 previously reported method.^{1,11,55,57} The RH values were 224 selected as a benchmark based on sucrose that shows solid to 225 semisolid and semisolid to liquid phase transitions at ~20 and 226 60% RH, respectively.^{1,11,55,57} A maximum force of 20 nN and 227 scan rate of 1 Hz were used.^{1,11} At least five force plots were 228 collected by probing at the shell region of core–shell and at 229 approximately the center of the rounded aged SSA.¹ The 230 collected force plots were then used to quantify the viscoelastic 231 response distance (VRD, nm) and the relative indentation 232 depth (RID, the ratio of the indentation distance over the 233 particle height) for an individual particle.^{11,55} The single- 234 particle phase state identification was conducted using an 235 established framework from VRD and RID measurements, as 236 described in prior studies.^{1,11,55,57} The VRD values measured 237 on aged SSA in the semisolid phase state were reported as an 238 average and one standard deviation. Approximately 10 or more 239 individual aged SSAs for each morphology were investigated. 240 The VRD values and relative abundance (i.e., an average and 241 one standard deviation for fraction of particles) of phase states 242 for the shell of core–shell SSA and rounded particles were 243 recorded at three volume-equivalent diameter ranges of 0.10– 244 0.18, 0.18–0.32, and 0.32–0.60 μm . The observations on

245 phase states and water uptake of aged SSA were compared with 246 the nSSA results reported previously.¹

247 **AFM–PTIR Measurements of Aged SSA Composition 248 at ~20–30% RH.** AFM–PTIR spectroscopic measurements 249 were collected using a commercial AFM-IR microscope 250 (nanoIR2, Bruker) with a tunable mid-IR quantum cascade 251 laser (QCL MIRcat-QT, Daylight solutions). Images and 252 spectra were collected at ~20–30% RH and ambient 253 temperature (23–26 °C) and pressure on individual aged 254 SSA deposited on silicon substrates placed on MOUDI stages 255 7, 8, and 9. Analysis was conducted using silicon nitride probes 256 with a chromium-gold coating (HQ: NSC19/CR-AU, 257 MikroMasch, typical tip radius of curvature 35 nm, and a 258 nominal spring constant range of 0.05–2.3 N/m). AFM 259 imaging was conducted in the tapping mode at a scan rate of 260 0.5 Hz. AFM–PTIR spectra were collected with a nominal 261 spatial resolution below 35 nm and a spectral resolution of 5 262 cm^{-1} , co-averaging over 128 laser pulses per wavenumber.¹ A 263 reference spectrum was taken on the substrate and subtracted 264 from all corresponding spectra obtained on individual particles. 265 For core–shell-aged SSA, spectra were taken at the core and 266 shell particle regions, while for rounded aged SSA spectra were 267 taken at an approximate center of each particle. Even 268 accounting for differences in morphology, the large diversity 269 of spectra between the aged SSA is reflected in large variances 270 between particles. The PTIR results collected on aged SSA 271 were compared with the nSSA results, which were recorded in 272 a prior study.¹

273 **Bulk Measurements of nSSA and Aged SSA Size- 274 Dependent Organic and Inorganic Mass Fractions.** For 275 these measurements, nSSA and aged SSA samples were 276 collected simultaneously during the peak of the phytoplankton 277 bloom using five stage SIOUTAS Personal Cascade Impactors 278 (PCIS, SKC model 225–370; 50% aerodynamic diameter 279 range cutoff for each stage).¹ The top four stages consisted of 280 pre-baked 25 mm Al foil disks (0.25–0.50, 0.50–1.0, 1.0–2.5, 281 and >2.5 μm) and the last stage a pre-baked 37 mm quartz 282 fiber filter (QFF, PALL Life Sciences, <0.25 μm). The nSSA 283 were collected directly from the wave flume and aged SSA by 284 first oxidizing in the PAM-OFR using the conditions described 285 above prior to collection.^{1,2} Flow rates of 9 L/min and ~75– 286 95% RH were maintained, and all samples were stored frozen 287 at –20 °C until the analysis. Organic carbon (OC) was 288 measured via a thermal optical analyzer (Sunset Laboratories, 289 Forest Grove, OR) and common inorganic ions were separated 290 and quantified via high-performance ion exchange chromatog- 291 raphy with conductivity detection (Dionex ICSS000, Sunny- 292 vale, CA).^{12,69,70} A stainless-steel punch was used to sub 293 sample substrates, which were subsequently extracted in 4 mL 294 of ultrapure water (>18.2 MΩ·cm, Thermo Barnstead Easy 295 Pure II) and filtered (0.45 μm polypropylene, Whatman). 296 Inorganic mass was estimated as the sea salt using the 297 measured mass of sodium converted to the mass of the sea salt 298 via a sodium/sea salt ratio of 3.26, as described previously.⁷¹

■ RESULTS AND DISCUSSION

299 **Impact of Atmospheric Aging on Bulk Organic 300 Enrichment in nSSA.** The bulk ensemble-averaged method 301 that was previously reported was used to investigate the size- 302 dependent organic enrichment in SSA samples.^{1,61} Figure 1A,B 303 shows the size-dependent bulk organic and inorganic mass 304 fractions in nSSA and aged SSA, respectively. Both samples 305 showed an increase in the organic mass fraction with 306

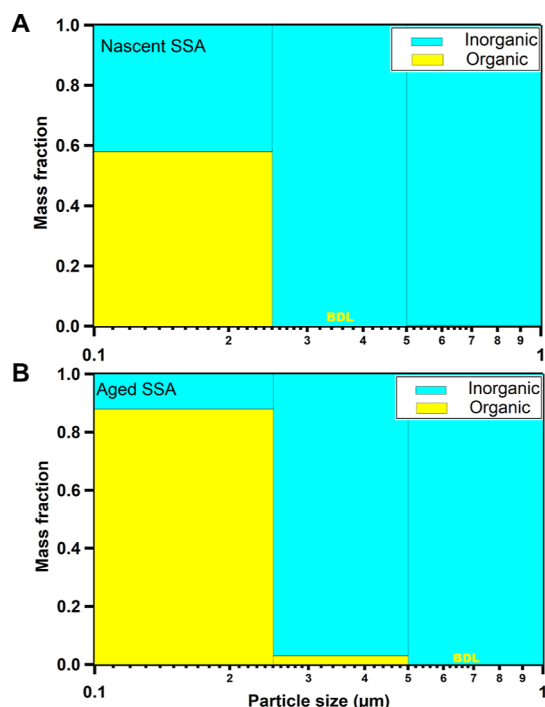


Figure 1. Organic (yellow) and inorganic (cyan) mass fractions versus particle size for (A) nascent and (B) aged SSA samples. The width of each bar indicates the SIOUTAS Personal Cascade Impactor cutoff size range at 74–96% RH. BDL indicates the measured organic mass fraction was below the detection limit. Organic and inorganic mass fractions for nascent SSA were adapted from Kaluarachchi et al., 2022.¹ Copyright 2022 American Chemical Society.

decreasing particle size, consistent with previous mesocosms and laboratory studies on nSSA.^{1,2,61} The relative uncertainty in the organic mass fraction measurement for the smallest size range nSSA and aged SSA were estimated to be 30–34 and ~30%, respectively. In addition, atmospheric aging increases the organic mass fraction in aged SSA across all sizes. Aged SSA with sizes below 0.25 μm showed the highest (~30%) increase of organic mass fraction relative to nSSA of similar sizes. The overall relative increase in the organic mass fraction can be attributed to the oxidation of volatile organic compounds in PAM-OFR followed by condensation on pre-existing particle or new particle formation.^{1,2,36,38,39,72} An increase in the organic mass fraction and possible changes in the composition of organic compounds in aged SSA as a result of atmospheric aging are expected to influence their physical–chemical properties, such as water uptake and phase state.^{3,39,43,44,50,72} For example, studies have shown that aging can result in an increase of oxygenated functional groups (e.g., hydroxyls and carbonyls) on parent particles, which in turn increases their hygroscopicity.^{39,72,73} Noteworthy, the size-dependent bulk organic enrichment in aged SSA relative to nSSA provides an ensemble-averaged value of an entire population of aerosols within a particular size range; however, it does not fully explain the origin of such enrichment nor provide an assessment on a possible particle-to-particle variability in the organic enrichment. Thus, single-particle measurements were next utilized to further assess the effects of aging on the nSSA composition and morphology and then supplemented with single-particle phase state and water uptake measurements.

Impact of Atmospheric Aging on Size-Dependent Morphological Distribution of nSSA. AFM single-particle imaging at ~20% RH was used to investigate substrate-

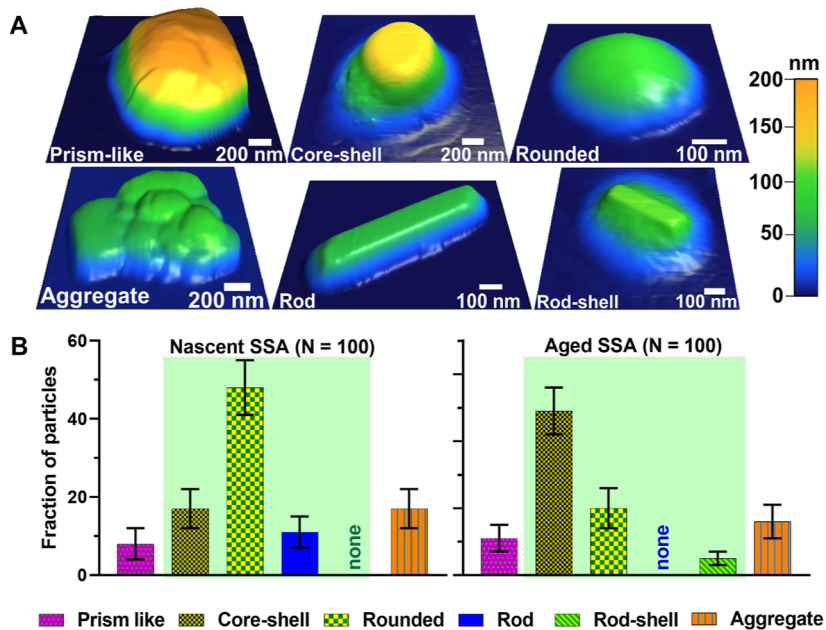


Figure 2. (A) Selected illustrative AFM 3D height images of six observed morphological categories (prism-like, core–shell, rounded, rod, rod–shell, and aggregate) for nascent and aged SSA samples. The maximum height range is 200 nm for each image. (B) Average and one standard deviation of fraction of particles (%) from six morphological categories for nascent (left) and aged (right) SSA for a total number of particles (N) 100 within the volume-equivalent diameter range of 0.10–0.60 μm . The term “none” indicates the absence of a particular morphology type (i.e., no rod–shells for nascent SSA, and no rods for aged SSA). Statistically significant differences of morphological categories are highlighted by green areas. AFM 3D-height image of rod and rounded SSA, and histogram for nascent SSA was adapted from Kaluarachchi et al., 2022.¹ Copyright 2022 American Chemical Society.

340 deposited aged SSA morphologies. Figure 2A shows
 341 representative AFM 3D height images of five main aged SSA
 342 morphological categories identified here (prism-like, core–
 343 shell, rounded, rod–shell, and aggregate) within a volume-
 344 equivalent diameter range of 0.10–0.60 μm . The categor-
 345 ization of morphologies was conducted qualitatively using
 346 AFM 3D height and phase images, as described previ-
 347 ously.^{1,12,55,57,61} The aged SSA morphologies were compared
 348 with nSSA morphologies (prism-like, core–shell, rounded, rod,
 349 and aggregate) reported previously for the same sampling day.¹
 350 Overall, both nSSA and aged SSA samples had particles with
 351 core–shell, prism-like, rounded, and aggregate morphologies.
 352 However, the rod morphology was only observed for nSSA,
 353 while the rod–shell morphology was only observed for aged
 354 SSA. As will be shown in the next section using AFM–PTIR,
 355 the rod particles were predominantly inorganic sulfates, while
 356 the rod–shell had inorganic sulfate rods with a predominantly
 357 organic shell. Therefore, it is likely that the organic shell in the
 358 rod–shell was formed from the condensation of volatile
 359 organic compounds onto pre-existing rods during the aging
 360 process of nSSA.

361 Figure 2B shows the relative distribution of main
 362 morphological categories for nSSA versus aged SSA over the
 363 same volume-equivalent size range of 0.10–0.60 μm . The
 364 relative distribution of each morphological type was assessed
 365 by performing statistical probability distribution analysis, as
 366 shown in prior studies.¹ From this analysis, we established
 367 statistically significant differences in the relative abundance of
 368 four main morphological categories—rounded, core–shell,
 369 rod, and rod–shell. Specifically, due to atmospheric aging, the
 370 relative abundance of rounded and rod SSA decreased from 48
 371 to 20% and from 11% to none, respectively. In contrast, the
 372 relative abundance of core–shell and rod–shell SSA increased
 373 from 17 to 49% and from none to 5%, respectively. While the
 374 exact origin for the observed morphological changes remains
 375 unknown, it is likely originating from a combination of several
 376 factors. First, organic compounds in nSSA likely became more
 377 oxygenated and some more volatile, which could explain an
 378 observed decrease in the relative abundance of rounded SSA
 379 that are predominantly organic.^{1,39,47,72,74} Second, semi-volatile
 380 or low-volatility organic compounds can condense onto pre-
 381 existing particles, leading to the formation of more core–shell
 382 particles (i.e., condensation onto prisms or core–shells) or
 383 formation of rod–shells (i.e., condensation onto
 384 rods).^{39,47,74–77} Third, the formation of more oxygenated
 385 organic compounds in aged SSA likely decreases their viscosity,
 386 which in turn can facilitate a more defined phase separation of
 387 organic and inorganic compounds within substrate-deposited
 388 particles, that can be more readily observed with AFM.^{46,61,72}
 389 Overall, our single-particle results clearly demonstrate that the
 390 atmospheric aging leads to changes in the relative abundance
 391 of SSA morphologies with a significant increase in the core–
 392 shells.

393 Figure 3A,B shows the size-dependent relative distribution
 394 of morphological categories of nSSA and aged SSA within
 395 three selected volume-equivalent diameter ranges of 0.10–
 396 0.18, 0.18–0.32, and 0.32–0.60 μm , respectively. The
 397 statistical probability distribution analysis to assess the
 398 significance in the distribution of morphological types across
 399 the size ranges was conducted as described in prior studies.¹
 400 For both sample types, as the particle size decreases, a
 401 significant increase in the relative abundance of rounded
 402 particles and a concurrent but smaller decrease of core–shells

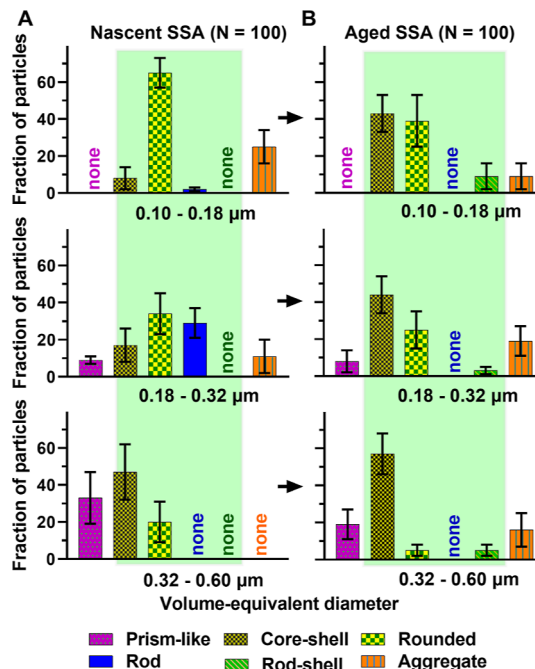


Figure 3. Relative distribution of the observed morphological categories (prism-like, core–shell, rounded, rod, rod–shell, and aggregate) of (A) nascent vs (B) aged SSA for a total number of particles (N) of 100, at three selected volume-equivalent diameter ranges of 0.10–0.18, 0.18–0.32, and 0.32–0.60 μm . The term “none” indicates absence of a particular morphology type within a specific subpopulation of SSA. Arrows are for illustrative purposes only and show changes in the morphological distribution from nascent to aged SSA within a particular volume-equivalent diameter range. Statistically-significant differences between nascent and aged SSA for size-dependent morphological categories are highlighted by green areas. The relative distribution of the morphological categories for nascent SSA was adapted from Kaluarachchi et al., 2022.¹ Copyright 2022 American Chemical Society.

was observed.¹ Additionally, for each size range, aged SSA had a higher abundance of core–shell particles as compared to nSSA. Moreover, for both samples, a prism-like morphology was predominantly observed at the largest size range. The relative abundances of rod and rod–shell particles were varying with respect to the particle size but without an apparent trend.

Figure 4 and Table 1 show the AFM-based single particle size-dependent organic volume fraction (OVF) and corresponding organic coating thickness (OCT) measurements for core–shell-aged SSA. Additionally, Figure 4 shows the size-dependent OVF values recorded for nSSA core–shells.¹ Based on the average OVF results, the corresponding average and one standard deviation of OCT were calculated for aged SSA core–shells, and the results were compared with previously recorded data for nSSA.¹ Overall, as the particle size decreases, the average core–shell OVF for nSSA increased from 0.18 ± 0.06 to 0.47 ± 0.09 , while that for aged SSA increased from 0.31 ± 0.21 to 0.57 ± 0.25 .¹ As the OCT values do not display any clear size dependency, the average value over the entire studied size range of 0.1–0.6 μm can be used to assess the effect of aging on the shell thickness. Specifically, the average and one standard deviation of core–shell OCT for nSSA was 16 ± 6 nm, while that for aged SSA was 24 ± 13 nm.

As will be demonstrated in the next section using AFM–PTIR spectroscopy, the core and shell regions of core–shell-aged SSA and nSSA are predominantly enriched with inorganic

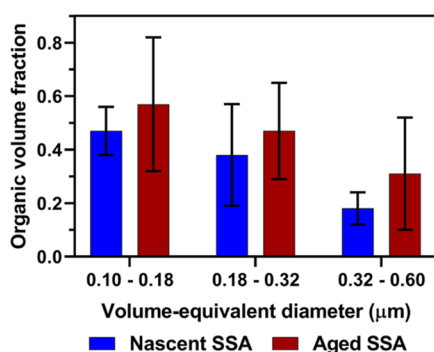


Figure 4. Averaged organic volume fraction measured using AFM at $\sim 20\%$ RH for core–shell individual SSA from nascent (blue) and aged (brown) samples at three selected volume-equivalent diameter ranges of $0.10\text{--}0.18$, $0.18\text{--}0.32$, and $0.32\text{--}0.60\ \mu\text{m}$. Each color bar height and error bar represent the average and one standard deviation, respectively. The OVF for nascent SSA were adapted from Kaluarachchi et al., 2022.¹ Copyright 2022 American Chemical Society.

and organic compounds, respectively.¹ Therefore, the larger OVF and OCT values are indicative of a relatively higher organic content in the core–shell particles.^{1,2,18,61} For both nSSA and aged SSA core–shells, a significant increase of the average OVF with the decreasing particle size was observed, which indicates significant organic enrichment in smaller particles.¹ In addition, compared to nSSA, aged SSA core–shells showed a significantly higher OVF and OCT values for all sizes, which indicates substantial organic enrichment as a result of atmospheric aging. Collectively, the observed bulk organic mass fraction enrichment in the smaller aged SSA (Figure 1 and corresponding discussion above) could be therefore attributed to a combination of an increase in OVF for

smaller core–shell particles and increased abundance of smaller predominantly organic rounded particles. Additionally, the observed increase of bulk organic mass fraction of aged SSA relative to nSSA (Figure 1) is likely due to a significant increase in the abundance of core–shell particles with a higher organic content.⁴⁴⁷

Changes in Single-Particle nSSA Composition due to Atmospheric Aging.

Figure 5A,B shows the AFM–PTIR spectra collected on nSSA and aged SSA core–shell particles at the core and shell regions. The core of nSSA core–shell particles are comprised IR inactive compounds, such as NaCl or contain nitrates [$\nu_{\text{as}}(\text{NO}_3^-)$: $1400, 1380\ \text{cm}^{-1}$], while the shells are enriched with aliphatic-rich compounds [$\delta(\text{CH}_2, \text{CH}_3)$: $1450, 1370\ \text{cm}^{-1}$].¹ A small shoulder at $\delta(\text{CH}_2)$: $1450\ \text{cm}^{-1}$ and modes around $\nu(\text{C–O, C–C})$: 1150 and $1050\ \text{cm}^{-1}$ are evident in spectra from the nSSA core, suggesting a thin layer of organic coating.¹ The aged SSA core–shells are spectrally distinct relative to nSSA core–shells. The core of the aged SSA core–shell is largely IR inactive from 800 to $1800\ \text{cm}^{-1}$. The shell of aged SSA core–shell is more functionalized in comparison to the nascent shells, as indicated by the larger vibrational mode around $1600\ \text{cm}^{-1}$, a broad mode that could have overlapping contributions from $\nu_{\text{as}}(\text{COO}^-)$, $\nu(\text{C=O})$, or even amides.^{78,79} Thus, based on the PTIR spectral comparison, the shell region of aged SSA is enriched with more oxygenated organic compounds relative to nSSA and provides a confirmation of the hypothesis that following OH oxidation, oxygenated gases partition to the surface of existing particles whereby the organic fraction increases with aging.⁴⁷⁰

Figure 5C,D shows the PTIR spectra collected on nSSA and aged SSA-rounded particles at the approximate center of individual particles. For both sample types, there are two similar large modes at $1415\text{--}1435\ \text{cm}^{-1}$ corresponding to aliphatic-rich compounds [$\delta(\text{CH}_2, \text{CH}_3)$] and oxygenated

Table 1. Summary of Core–Shell and Rounded Aged SSA Properties for Three Selected Volume-Equivalent Diameter Ranges of $0.10\text{--}0.18$, $0.18\text{--}0.32$, and $0.32\text{--}0.60\ \mu\text{m}$ During the Phytoplankton Bloom Including an Averaged and One Standard Deviation for Fraction of Particles at Solid, Semisolid, and Liquid Phase States at 20 and 60% RH, VRD for the Semisolid Shell of Core–shell and Semisolid Rounded Particles, OVF, and Corresponding OCT for Core–shell Particles, Volume-Equivalent GF, and Hygroscopicity Parameter (κ_{Mix})

Diameter range (μm)	Fraction of particles at specified phase state (%)					OVF	OCT (nm)	GF (80% RH)	κ_{Mix} (80% RH)
	RH (%)	Solid	Semisolid	Liquid	VRD ^a (nm)				
Core-shell									
<i>0.10 – 0.18</i>	20	0	100	0	2.1 ± 0.8	0.57 ± 0.25	23 ± 16	NA	NA
	60	0	100	0	4.6 ± 2.9				
<i>0.18 – 0.32</i>	20	0	100	0	2.3 ± 1.3	0.47 ± 0.18	25 ± 12	NA	NA
	60	0	89 ± 5	11 ± 4	3.3 ± 1.3				
<i>0.32 – 0.60</i>	20	0	100	0	2.7 ± 1.8	0.31 ± 0.21	25 ± 12	1.4 ± 0.3	0.5 ± 0.4
	60	0	83 ± 6	17 ± 5	4.5 ± 2.6				
Rounded									
<i>0.10 – 0.18</i>	20	0	100	0	1.3 ± 0.5	NA	NA	1.1 ± 0.1	0.1 ± 0.1
	60	0	100	0	1.5 ± 0.4				
<i>0.18 – 0.32</i>	20	0	100	0	3.3 ± 3.8	NA	NA	NA	NA
	60	0	100	0	4.0 ± 2.5				
<i>0.32 – 0.60</i>	20	0	100	0	1.1 ± 0.4	NA	NA	NA	NA
	60	0	100	0	4.2 ± 1.0				

^aData range reported by probing shell region of core–shell, and the center of rounded aged SSA at the semisolid phase state. Statistically significant differences for a particular property are highlighted by green areas.

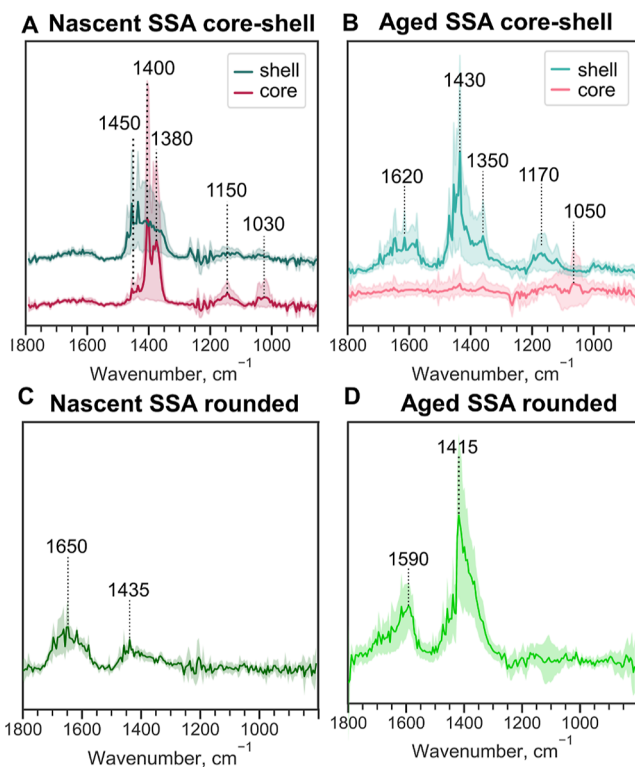


Figure 5. PTIR spectra for (A) nascent and (B) aged core–shell SSA, (C) nascent and (D) aged rounded SSA within the volume-equivalent diameter range of 0.10–0.60 μm . Spectra were taken at core and shell regions for core–shell SSA, and at approximately particle center for rounded SSA. Solid lines show the averaged spectra (number of individual core–shell SSA ≥ 10 , and number of individual rounded SSA ≥ 10) and shaded lines represent the 95% confidence interval. The spectra for nascent SSA were adapted from Kaluarachchi et al., 2022.¹ Copyright 2022 American Chemical Society.

476 functional groups $\nu(\text{COO}^-)$] and around 1600 cm^{-1} that
 477 could have overlapping contributions from $\nu_{\text{as}}(\text{COO}^-)$, $\nu(\text{C}=\text{O})$, or even amides.^{78,79} While relative intensities of these two
 478 main modes somewhat differ which may indicate variability of
 479 different functional groups, the presence of two modes for both
 480 samples suggests similar functional groups are present for both
 481 samples. Additionally, the PTIR spectra for rounded aged SSA
 482 appear to be spectrally similar to the shell region of core–shell–
 483 aged SSA, suggesting the presence of similar functional groups
 484 for these samples. We note, due to large chemical diversity
 485 within SSA, combined single-particle PTIR spectra show a
 486 large variance. Thus, spectral results presented herein
 487 demonstrate the presence (or potential absence) of a particular
 488 functional group within SSA.¹

489 **Figure 6A,B** shows the AFM 3D height image and zoomed
 490 in the region for the aged SSA rod–shell particles, where
 491 AFM–PTIR spectra were taken. PTIR spectra shown in **Figure**
 492 **6C** reveals that the rod is inorganic sulfate, similar to rod–
 493 particles observed on the nSSA sample,¹ as evidenced by the
 494 $\nu_{\text{as}}(\text{SO}_4^{2-})$ mode at 1170 cm^{-1} .⁸⁰ The shell region of rod–
 495 shells is organically rich with a distinct mode of $\nu(\text{C}=\text{O})$ at
 496 1700 cm^{-1} .^{81,82} Hyperspectral maps of the particle (**Figure**
 497 **6D**) show the spatial distribution of absorbances within
 498 100 cm^{-1} integrated spectral bins. The rod-shaped core of the
 499 particle only has absorbances consistent with the sulfate
 500 (1100–1200 cm^{-1}), while the shell is more intensely absorbing
 501 in spectral maps for other spectral regions such as $\delta(\text{CH}_3)$,

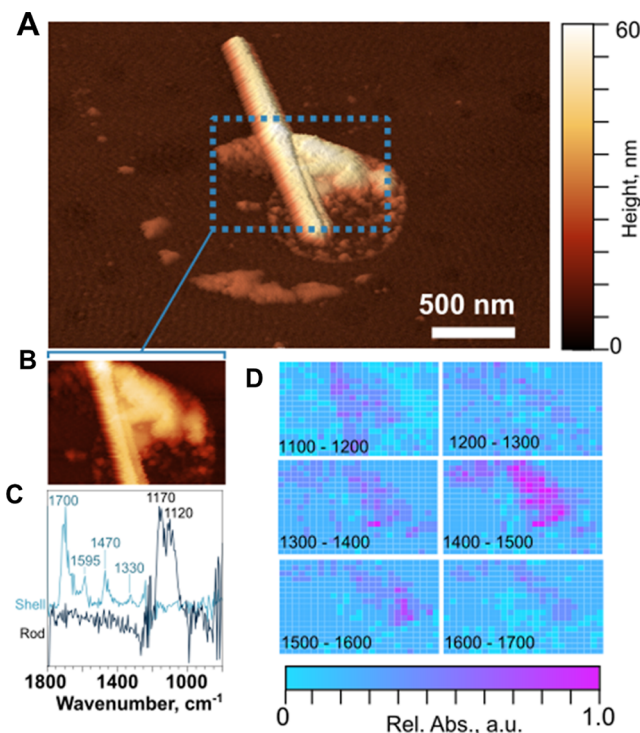


Figure 6. (A) AFM 3D height image and (B) zoomed in region of the aged rod–shell particle with (C) AFM–PTIR spectra measured over the rod (black line) and shell (blue line) regions and (D) hyperspectral maps recorded over the rod–shell particle shown over 1100–1700 wavenumber range with 100 cm^{-1} windows.

CH_2): 1330, 1470 cm^{-1} , $\nu_{\text{as}}(\text{COO}^-)$: 1570 cm^{-1} , $\nu(\text{C}=\text{C})$: 503 1595 cm^{-1} , and $\nu(\text{C}=\text{O})$: 1700 cm^{-1} . It is likely that the rod–
 504 shell particles were formed due to the condensation of semi-
 505 volatile or low volatility oxygenated organic compounds on
 506 pre-existing rod particles during the heterogeneous aging
 507 process in PAM-OFR.^{81–83} Furthermore, the PTIR spectra for
 508 the shell region of core–shell– and rod–shell–aged SSA and
 509 rounded aged SSA appear to be comparable, suggesting the
 510 presence of similar organic functional groups. Formation of
 511 more oxygenated organic species in aged SSA core–shells
 512 relative to nSSA core–shells could potentially influence
 513 particle phase state and hygroscopicity as discussed below.⁵¹⁴

Influence of Atmospheric Aging on Phase State and Water Uptake of Rounded and Core–Shell nSSA. Phase state identification on the highest abundance morphologies (i.e., core–shell and rounded) of aged SSA were performed at 20 and 60% RH using the AFM force spectroscopy (i.e., force profiles).^{1,11,55,57} At least five repeated force profiles were collected by probing at the shell region of each core–shell and at an approximate particle center for each rounded particle. The measurements over the core of aged SSA core–shell particles were not reported because it is solid with possibly a thin organic layer, as shown in our prior studies.¹ The force profiles were then used to quantify VRD (nm, viscoelastic response distance) and RID (ratio of the indentation depth over the particle height) for an individual particle at a particular RH and determine phase states using previously established frameworks based on these measurements.^{1,11,55,57} Previous studies showed that the VRD values can be related to the viscoelastic nature of particles, where higher values generally correspond to lower viscosity.^{1,11,57} **Table 1** shows the VRD values measured on semisolid particles within three

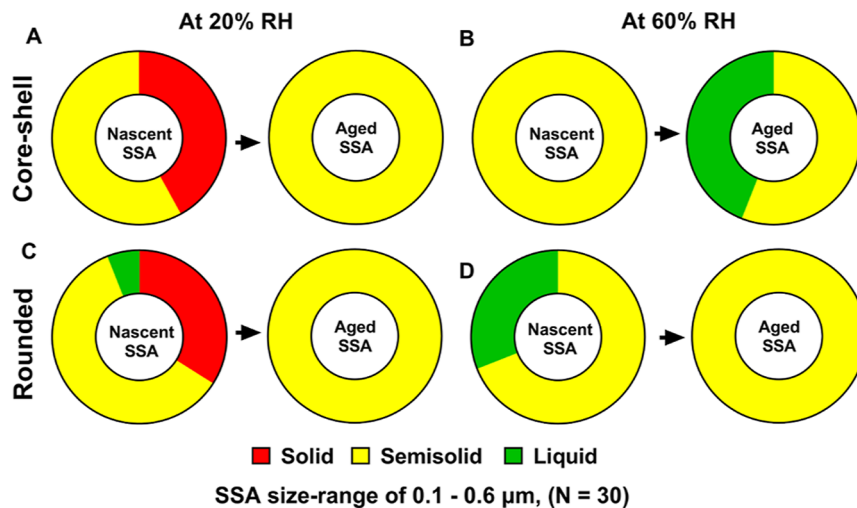


Figure 7. Relative distributions of solid, semisolid, and liquid phase states for (A,B) shell region of nascent and aged SSA core–shell at 20 and 60% RH, respectively (C,D) nascent and aged SSA rounded at 20 and 60% RH, respectively. SSA are within the volume-equivalent diameter range of 0.10–0.60 μm . Arrows are for illustrative purposes only. The phase state information for nascent SSA were adapted from Kaluarachchi et al., 2022.¹ Copyright 2022 American Chemical Society.

selected volume-equivalent diameter ranges of 0.10–0.18, 0.18–0.32, and 0.32–0.60 μm . A statistical probability distribution analysis on solid, semisolid, and liquid phase states for the shell region of core–shell and rounded aged SSA were performed, as described in previous studies.¹ Because no apparent size-dependent phase state was observed for core–shells and rounded aged SSA, the phase state results for each particle type were combined over a wider volume-equivalent diameter range of 0.1–0.6 μm .

Figure 7A,B shows the relative distributions of solid, semisolid, and liquid phase states for the shell region of aged SSA versus nSSA core–shells. At 20% RH, nSSA had either solid or semisolid shells, while aged SSA had only semisolid shells. Furthermore, the VRD values measured on aged SSA semisolid shells were greater than that for nSSA, which is likely indicative of lower shell viscosity as a result of atmospheric aging.¹ The results were consistent with the presence of more oxygenated organic compounds, as evident by the PTIR measurements discussed above. As RH increased to 60%, aged SSA shells became hydrated and a significant fraction of shells were liquid, while nSSA shells were only semisolid.¹ Collectively, due to the aging, the phase state of shells shifted toward a more semisolid state (likely with lower viscosity) within the considered RH range.

Figure 7C,D shows the relative distributions of solid, semisolid, and liquid phase states for rounded aged SSA versus nSSA. Specifically, at 20% RH, rounded nSSAs were either solid or semisolid, while rounded aged SSA were only semisolid.¹ However, the VRD values measured on semisolid rounded nSSA versus aged SSA did not show a significant variability, which was consistent with the presence of similar functional groups for each sample, as evident by the PTIR measurements discussed above. As RH increased to 60%, rounded aged SSA only showed a semisolid phase state, while the majority of nSSA rounded was semisolid with a small fraction as a liquid.¹

The 3D growth factor (GF) and corresponding hygroscopicity parameter (κ_{mix}) of core–shell and rounded aged SSA were determined at 80% RH using a previously reported approach, and the corresponding average and one standard

deviation values are reported in Table 1.^{1,11,67,68,84} The measurements were performed on the core–shell and rounded aged SSA at the highest relative occurrence size ranges of 0.32–0.60 and 0.10–0.18 μm , respectively. Specifically, the GF (range 1.2–1.7) and κ_{mix} (average 0.5 ± 0.4) values for aged SSA core–shells were higher compared to the GF (range 1.2–1.4) and κ_{mix} (average 0.3 ± 0.2) values of nSSA core–shells for similar sizes as reported by us previously.¹ An increase in hygroscopicity and water uptake observed on the aged SSA core–shells relative to nSSA core–shells is consistent with the AFM–PTIR spectral data and AFM phase state measurements, which showed formation of more oxygenated organics and increasing the relative abundance of liquid shells as a result of aging. In contrast, there is no apparent difference in the nSSA–rounded particle GF (range 1.0–1.2) and κ_{mix} (average 0.1 ± 0.1) values and aged SSA–rounded particle GF (range 1.0–1.2) and κ_{mix} (average 0.1 ± 0.1) values. These results are consistent with AFM–PTIR measurements described above, where spectra for these two samples suggest the presence of similar functional groups.

SUMMARY AND IMPLICATIONS

Atmospheric aging can alter various physicochemical properties of the SSA.^{36–39,74,85,86} The current study investigated the effects of atmospheric aging of nSSA (i.e., oxidation with OH radicals corresponds to 4–5 days of atmospheric aging) on their size-dependent morphology, composition, water uptake, phase state, and particle-to-particle variability of these properties, for submicron nSSA and aged SSA collected during a mesocosm study. As is evident by filter-based measurements, both nSSA and aged SSA showed an increase in the organic mass fraction with decreasing particle size. In addition, aging further increased the organic mass fraction in aged SSA. These results can be rationalized with complementary single-particle measurements presented here, which showed a relative increase in the abundance of aged SSA core–shells with significantly higher organic coating thickness, compared to nSSA. Additionally, as is evident by PTIR spectra, aged SSA core–shells contained relatively more oxygenated organic species than nSSA. We also noticed a significant particle-to-

614 particle variability in the aged SSA organic content and
615 composition. Aged SSA morphology, organic content, and
616 composition can influence their direct and indirect aerosol
617 effects (e.g., scattering, water uptake, CCN, and IN
618 efficiency).^{13,26,87,88} For example, prior studies showed core–
619 shells can undergo atmospheric aging within days, while
620 rounded particles can take up to weeks or months.^{36,52} The
621 organic coating thickness of core–shells can further control the
622 diffusion time scale of gas phase molecules in the atmosphere,
623 that is, thicker coating can significantly increase the diffusion
624 time into the particle.^{36,89} Moreover, as demonstrated in the
625 current study, aged SSA morphology and organic content can
626 modify their hygroscopicity by the presence of water-soluble or
627 insoluble compounds.^{1,11,46,55,62} In particular, higher hygro-
628 scopicity and more efficient water uptake properties were
629 observed for aged SSA core–shells, which had more
630 oxygenated organic species relative to nSSA core–shells,
631 while rounded aged SSA and rounded nSSA had similar
632 water uptake properties and no apparent changes in the
633 composition. The aged SSA morphology and composition-
634 induced water uptake can modify their sizes and affect the
635 direct and indirect aerosol properties.^{1–3,11,26,27,68,90}

636 Atmospheric aging increased the abundance of core–shells
637 at the semisolid or liquid phase state, while nSSA core–shells
638 were primarily solid or semisolid (RH range of 20–60%). The
639 results can be compared with prior reports conducted on aged
640 SSA model systems. For example, a study conducted on model
641 organic aerosols showed a significant enhancement of the
642 particle hygroscopicity upon exposure to OH radicals that were
643 initially hydrophobic.^{43,46,49} Another study showed that the
644 atmospheric aging of model aerosol particles can potentially
645 increase the particle hygroscopicity, thus the formation of more
646 semisolid or liquid particles even at dry RH conditions, which
647 agreed with our observations from the current study.^{74,91}

648 Particle phase state and hygroscopicity can control their
649 indirect aerosol effects, where liquid droplets can be better
650 CCN while solid particles can be better
651 IN.^{1,3,11,26,27,55,58,68,92,93} Thus, aged SSA in the liquid phase
652 state can likely show an enhanced CCN ability compared to
653 nSSA at the solid phase state.^{36–39,72} Furthermore, the particle
654 phase state can alter the bulk diffusion of small molecules (e.g.,
655 water, nonvolatile organic species), and characteristic time for
656 their mass-transport and mixing by molecular diffusion in the
657 aged SSA.^{74,85,86,89} For example, diffusion time required for
658 small molecules in a solid particle is much higher (~years)
659 than that of a semisolid (~seconds).^{76,89,94–96} As demon-
660 strated in the current study, the VRD values measured on
661 shells of aged SSA core–shells were shifted toward relatively
662 higher values, which likely indicated that the aged SSA shells
663 were becoming less viscous due to the aging.

664 Overall, our results illustrate that atmospheric aging results
665 in significant changes in SSA morphology, composition, phase
666 state, and water uptake properties. Significantly, these changes
667 are not the same for the entire SSA population but rather show
668 a significant particle-to-particle variability and size-dependency.
669 These findings highlight the importance of single-particle
670 methods that are complementary to bulk ensemble-average
671 approaches and support the premise that future studies aiming
672 to better understand and model the effects of atmospheric
673 aging of SSA should account for possible aerosol size effects
674 and particle-to-particle variability.

■ AUTHOR INFORMATION

Corresponding Author	676
Alexei V. Tivanski – Department of Chemistry, University of Iowa, Iowa City, Iowa 52242, United States;  orcid.org/0000-0002-1528-2421 ; Email: alexei-tivanski@uiowa.edu	677
Authors	680
Chathuri P. Kaluarachchi – Department of Chemistry, University of Iowa, Iowa City, Iowa 52242, United States;  orcid.org/0000-0003-2538-3952	681
Victor W. Or – Department of Chemistry and Biochemistry, University of California, San Diego, California 92093, United States	684
Yiling Lan – Department of Chemistry, University of Iowa, Iowa City, Iowa 52242, United States	687
Elias S. Hasenecz – Department of Chemistry, University of Iowa, Iowa City, Iowa 52242, United States	689
Deborah Kim – Department of Chemistry and Biochemistry, University of California, San Diego, California 92093, United States;  orcid.org/0000-0001-6717-8397	691
Chamika K. Madawala – Department of Chemistry, University of Iowa, Iowa City, Iowa 52242, United States	694
Glorianne Dorcé – Department of Chemistry, University of Iowa, Iowa City, Iowa 52242, United States	696
Kathryn J. Mayer – Department of Chemistry and Biochemistry, University of California, San Diego, California 92093, United States	698
Jonathan S. Sauer – Department of Chemistry and Biochemistry, University of California, San Diego, California 92093, United States	701
Christopher Lee – Scripps Institution of Oceanography, University of California, San Diego, California 92093, United States	704
Christopher D. Cappa – Department of Civil and Environmental Engineering, University of California, Davis, California 95616, United States;  orcid.org/0000-0002-3528-3368	707
Timothy H. Bertram – Department of Chemistry, University of Wisconsin–Madison, Madison, Wisconsin 53706, United States	711
Elizabeth A. Stone – Department of Chemistry, University of Iowa, Iowa City, Iowa 52242, United States;  orcid.org/0000-0003-0078-141X	714
Kimberly A. Prather – Department of Chemistry and Biochemistry and Scripps Institution of Oceanography, University of California, San Diego, California 92093, United States	717
Vicki H. Grassian – Department of Chemistry and Biochemistry and Scripps Institution of Oceanography, University of California, San Diego, California 92093, United States;  orcid.org/0000-0001-5052-0045	721
Complete contact information is available at: https://pubs.acs.org/10.1021/acsearthspacechem.2c00258	725
Author Contributions	727
The manuscript was written through contributions of all authors. All authors have given approval to the final version of the manuscript. Project administration: K.A.P., V.H.G., C.D.C., T.H.B., C.L., E.A.S., and A.V.T. Sample and data collection: C.P.K., V.W.O., Y.L., E.S.H., D.R.C., C.K.M., and D.K. Writing: C.P.K., V.W.O., E.S.H., D.K., E.A.S., T.H.B., V.H.G., and A.V.T.	728
	729
	730
	731
	732
	733
	734

735 Notes

736 The authors declare no competing financial interest.

737 ■ ACKNOWLEDGMENTS

738 This work was funded by the National Science Foundation
739 (NSF) through the NSF Center for Aerosol Impacts on
740 Chemistry of the Environment (CAICE) under grant no.
741 CHE-1801971. The authors thank Prof. Christopher Cappa for
742 providing the Igor-pro wave metric code to perform the
743 statistical analysis on probability distribution. Thank you to the
744 entire SeaSCAPE team, and especially Dr. Kathryn Mayer, Dr.
745 Jonathan Sauer, Dr. Christopher Lee, Prof. Timothy Bertram,
746 Prof. Christopher Cappa, and Prof. Kimberly Prather for
747 designing and overseeing the campaign. A full list of
748 participants can be found online: <https://caice.ucsd.edu/experiment-campaigns/>. C.P.K. was partially supported by a
750 University of Iowa Graduate College Summer Fellowship.

751 ■ REFERENCES

752 (1) Kaluarachchi, C. P.; Or, V. W.; Lan, Y.; Madawala, C. K.;
753 Hasenecz, E. S.; Crocker, D. R.; Morris, C. K.; Lee, H. D.; Mayer, K.
754 J.; Sauer, J. S.; Lee, C.; Dorce, G.; Malfatti, F.; Stone, E. A.; Cappa, C.
755 D.; Grassian, V. H.; Prather, K. A.; Tivanski, A. V. Size-Dependent
756 Morphology, Composition, Phase State, and Water Uptake of
757 Nascent Submicrometer Sea Spray Aerosols during a Phytoplankton
758 Bloom. *ACS Earth Space Chem.* **2022**, *6*, 116–130.

759 (2) Sauer, J. S.; Mayer, K. J.; Lee, C.; Alves, M. R.; Amiri, S.;
760 Bahaveolos, C. J.; Franklin, E. B.; Crocker, D. R.; Dang, D.;
761 Dinasquet, J.; Garofalo, L. A.; Kaluarachchi, C. P.; Kilgour, D. B.;
762 Mael, L. E.; Mitts, B. A.; Moon, D. R.; Moore, A. N.; Morris, C. K.;
763 Mullenmeister, C. A.; Ni, C.-M.; Pendergraft, M. A.; Petras, D.;
764 Simpson, R. M. C.; Smith, S.; Tumminello, P. R.; Walker, J. L.;
765 DeMott, P. J.; Farmer, D. K.; Goldstein, A. H.; Grassian, V. H.; Jaffe,
766 J. S.; Malfatti, F.; Martz, T. R.; Slade, J. H.; Tivanski, A. V.; Bertram,
767 T. H.; Cappa, C. D.; Prather, K. A. The Sea Spray Chemistry and
768 Particle Evolution study (SeaSCAPE): overview and experimental
769 methods. *Environ. Sci.: Processes Impacts* **2022**, *24*, 290.

770 (3) Cochran, R. E.; Laskina, O.; Trueblood, J. V.; Estillore, A. D.;
771 Morris, H. S.; Jayarathne, T.; Sultana, C. M.; Lee, C.; Lin, P.; Laskin,
772 J.; Laskin, A.; Dowling, J. A.; Qin, Z.; Cappa, C. D.; Bertram, T. H.;
773 Tivanski, A. V.; Stone, E. A.; Prather, K. A.; Grassian, V. H. Molecular
774 Diversity of Sea Spray Aerosol Particles: Impact of Ocean Biology on
775 Particle Composition and Hygroscopicity. *Chem.* **2017**, *2*, 655–667.

776 (4) Cochran, R. E.; Ryder, O. S.; Grassian, V. H.; Prather, K. A. Sea
777 Spray Aerosol: The Chemical Link between the Oceans, Atmosphere,
778 and Climate. *Acc. Chem. Res.* **2017**, *50*, 599–604.

779 (5) Cochran, R. E.; Laskina, O.; Jayarathne, T.; Laskin, A.; Laskin, J.;
780 Lin, P.; Sultana, C.; Lee, C.; Moore, K. A.; Cappa, C. D.; Bertram, T.
781 H.; Prather, K. A.; Grassian, V. H.; Stone, E. A. Analysis of Organic
782 Anionic Surfactants in Fine and Coarse Fractions of Freshly Emitted
783 Sea Spray Aerosol. *Environ. Sci. Technol.* **2016**, *50*, 2477–2486.

784 (6) Collins, D. B.; Bertram, T. H.; Sultana, C. M.; Lee, C.; Axson, J.
785 L.; Prather, K. A. Phytoplankton blooms weakly influence the cloud
786 forming ability of sea spray aerosol. *Geophys. Res. Lett.* **2016**, *43*,
787 9975–9983.

788 (7) Collins, D. B.; Zhao, D. F.; Ruppel, M. J.; Laskina, O.;
789 Grandquist, J. R.; Modini, R. L.; Stokes, M. D.; Russell, L. M.;
790 Bertram, T. H.; Grassian, V. H.; Deane, G. B.; Prather, K. A. Direct
791 aerosol chemical composition measurements to evaluate the
792 physicochemical differences between controlled sea spray aerosol
793 generation schemes. *Atmos. Meas. Tech.* **2014**, *7*, 3667–3683.

794 (8) Crocker, D. R.; Hernandez, R. E.; Huang, H. D.; Pendergraft, M.
795 A.; Cao, R.; Dai, J.; Morris, C. K.; Deane, G. B.; Prather, K. A.;
796 Thiemens, M. H. Biological Influence on $\delta^{13}\text{C}$ and Organic
797 Composition of Nascent Sea Spray Aerosol. *ACS Earth Space Chem.*
798 **2020**, *4*, 1686–1699.

799 (9) Hasenecz, E. S.; Jayarathne, T.; Pendergraft, M. A.; Santander,
800 M. V.; Mayer, K. J.; Sauer, J.; Lee, C.; Gibson, W. S.; Kruse, S. M.;
801 Malfatti, F.; Prather, K. A.; Stone, E. A. Marine Bacteria Affect
802 Saccharide Enrichment in Sea Spray Aerosol during a Phytoplankton
803 Bloom. *ACS Earth Space Chem.* **2020**, *4*, 1638–1649.

804 (10) Jayarathne, T.; Sultana, C. M.; Lee, C.; Malfatti, F.; Cox, J. L.;
805 Pendergraft, M. A.; Moore, K. A.; Azam, F.; Tivanski, A. V.; Cappa, C.
806 D.; Bertram, T. H.; Grassian, V. H.; Prather, K. A.; Stone, E. A. 807
807 Enrichment of Saccharides and Divalent Cations in Sea Spray Aerosol
808 During Two Phytoplankton Blooms. *Environ. Sci. Technol.* **2016**, *50*,
809 11511–11520.

810 (11) Lee, H. D.; Morris, H. S.; Laskina, O.; Sultana, C. M.; Lee, C.;
811 Jayarathne, T.; Cox, J. L.; Wang, X. F.; Hasenecz, E. S.; DeMott, P. J.;
812 Bertram, T. H.; Cappa, C. D.; Stone, E. A.; Prather, K. A.; Grassian, V.
813 H.; Tivanski, A. V. Organic Enrichment, Physical Phase State, and
814 Surface Tension Depression of Nascent Core-Shell Sea Spray
815 Aerosols during Two Phytoplankton Blooms. *ACS Earth Space*
816 *Chem.* **2020**, *4*, 650–660.

817 (12) Lee, H. D.; Wigley, S.; Lee, C.; Or, V. W.; Hasenecz, E. S.;
818 Stone, E. A.; Grassian, V. H.; Prather, K. A.; Tivanski, A. V. 819
819 Physicochemical Mixing State of Sea Spray Aerosols: Morphologies
820 Exhibit Size Dependence. *ACS Earth Space Chem.* **2020**, *4*, 1604–
821 1611.

822 (13) Prather, K. A.; Bertram, T. H.; Grassian, V. H.; Deane, G. B.;
823 Stokes, M. D.; DeMott, P. J.; Aluwihare, L. I.; Palenik, B. P.; Azam, F.;
824 Seinfeld, J. H.; Moffet, R. C.; Molina, M. J.; Cappa, C. D.; Geiger, F.
825 M.; Roberts, G. C.; Russell, L. M.; Ault, A. P.; Baltrusaitis, J.; Collins,
826 D. B.; Corrigan, C. E.; Cuadra-Rodriguez, L. A.; Ebbin, C. J.;
827 Forestieri, S. D.; Guasco, T. L.; Hersey, S. P.; Kim, M. J.; Lambert, W.
828 F.; Modini, R. L.; Mui, W.; Pedler, B. E.; Ruppel, M. J.; Ryder, O. S.;
829 Schoepp, N. G.; Sullivan, R. C.; Zhao, D. F. Bringing the ocean into
830 the laboratory to probe the chemical complexity of sea spray aerosol.
831 *Proc. Natl. Acad. Sci. U.S.A.* **2013**, *110*, 7550–7555.

832 (14) Crocker, D.; Deane, G. B.; Cao, R.; Santander, M. V.; Morris,
833 C. K.; Mitts, B. A.; Dinasquet, J.; Amiri, S.; Malfatti, F.; Prather, K. A.;
834 Thiemens, M. H. Biologically Induced Changes in the Partitioning of
835 Submicron Particulates Between Bulk Seawater and the Sea Surface
836 Microlayer. *Geophys. Res. Lett.* **2022**, *49*, No. e2021GL094587.

837 (15) Kaluarachchi, C. P.; Lee, H. D.; Lan, Y.; Lansakara, T. I.;
838 Tivanski, A. V. Surface Tension Measurements of Aqueous Liquid–
839 Air Interfaces Probed with Microscopic Indentation. *Langmuir* **2021**,
840 *37*, 2457–2465.

841 (16) Cochran, R. E.; Jayarathne, T.; Stone, E. A.; Grassian, V. H.
842 Selectivity Across the Interface: A Test of Surface Activity in the
843 Composition of Organic-Enriched Aerosols from Bubble Bursting. *J.*
844 *Phys. Chem. Lett.* **2016**, *7*, 1692–1696.

845 (17) Crocker, D. R.; Kaluarachchi, C. P.; Cao, R.; Dinasquet, J.;
846 Franklin, E. B.; Morris, C. K.; Amiri, S.; Petras, D.; Nguyen, T.;
847 Torres, R. R.; Martz, T. R.; Malfatti, F.; Goldstein, A. H.; Tivanski, A.
848 V.; Prather, K. A.; Thiemens, M. H. Isotopic Insights into Organic
849 Composition Differences between Supermicron and Submicron Sea
850 Spray Aerosol. *Environ. Sci. Technol.* **2022**, *56*, 9947–9958.

851 (18) Hasenecz, E. S.; Kaluarachchi, C. P.; Lee, H. D.; Tivanski, A.
852 V.; Stone, E. A. Saccharide Transfer to Sea Spray Aerosol Enhanced
853 by Surface Activity, Calcium, and Protein Interactions. *ACS Earth*
854 *Space Chem.* **2019**, *3*, 2539–2548.

855 (19) Alpert, P. A.; Kilthau, W. P.; Bothe, D. W.; Radway, J. C.; Aller,
856 J. Y.; Knopf, D. A. The influence of marine microbial activities on
857 aerosol production: A laboratory mesocosm study. *J. Geophys. Res.*
858 *Atmos.* **2015**, *120*, 8841–8860.

859 (20) Fuentes, E.; Coe, H.; Green, D.; de Leeuw, G.; McFiggans, G.
860 On the impacts of phytoplankton-derived organic matter on the
861 properties of the primary marine aerosol – Part 1: Source fluxes.
862 *Atmos. Chem. Phys.* **2010**, *10*, 9295–9317.

863 (21) Fuentes, E.; Coe, H.; Green, D.; McFiggans, G. On the impacts
864 of phytoplankton-derived organic matter on the properties of the
865 primary marine aerosol – Part 2: Composition, hygroscopicity and
866 cloud condensation activity. *Atmos. Chem. Phys.* **2011**, *11*, 2585–
867 2602.

868 (22) Fuentes, E.; Coe, H.; Green, D.; de Leeuw, G.; McFiggans, G.
869 Laboratory-generated primary marine aerosol via bubble-bursting and
870 atomization. *Atmos. Meas. Tech.* **2010**, *3*, 141–162.

871 (23) Schwier, A. N.; Rose, C.; Asmi, E.; Ebning, A. M.; Landing, W.
872 M.; Marro, S.; Pedrotti, M. L.; Sallou, A.; Iuculano, F.; Agusti, S.;
873 Tsiola, A.; Pitta, P.; Louis, J.; Guiieu, C.; Gazeau, F.; Sellegrí, K.
874 Primary marine aerosol emissions from the Mediterranean Sea during
875 pre-bloom and oligotrophic conditions: correlations to seawater
876 chlorophyll a from a mesocosm study. *Atmos. Chem. Phys.* **2015**, *15*,
877 7961–7976.

878 (24) Bertram, T. H.; Cochran, R. E.; Grassian, V. H.; Stone, E. A.
879 Sea spray aerosol chemical composition: elemental and molecular
880 mimics for laboratory studies of heterogeneous and multiphase
881 reactions. *Chem. Soc. Rev.* **2018**, *47*, 2374–2400.

882 (25) Ault, A. P.; Moffet, R. C.; Baltrusaitis, J.; Collins, D. B.; Ruppel,
883 M. J.; Cuadra-Rodriguez, L. A.; Zhao, D. F.; Guasco, T. L.; Ebbin, C.
884 J.; Geiger, F. M.; Bertram, T. H.; Prather, K. A.; Grassian, V. H. Size-
885 Dependent Changes in Sea Spray Aerosol Composition and
886 Properties with Different Seawater Conditions. *Environ. Sci. Technol.*
887 **2013**, *47*, 5603–5612.

888 (26) DeMott, P. J.; Hill, T. C. J.; McCluskey, C. S.; Prather, K. A.;
889 Collins, D. B.; Sullivan, R. C.; Ruppel, M. J.; Mason, R. H.; Irish, V.
890 E.; Lee, T.; Hwang, C. Y.; Rhee, T. S.; Snider, J. R.; McMeeking, G.
891 R.; Dhaniyala, S.; Lewis, E. R.; Wentzell, J. J. B.; Abbott, J.; Lee, C.;
892 Sultana, C. M.; Ault, A. P.; Axson, J. L.; Diaz Martinez, M. D.; Venero,
893 I.; Santos-Figueroa, G.; Stokes, M. D.; Deane, G. B.; Mayol-Bracero,
894 O. L.; Grassian, V. H.; Bertram, T. H.; Bertram, A. K.; Moffett, B. F.;
895 Franc, G. D. Sea spray aerosol as a unique source of ice nucleating
896 particles. *Proc. Natl. Acad. Sci. U.S.A.* **2016**, *113*, 5797–5803.

897 (27) Forestieri, S. D.; Cornwell, G. C.; Helgestad, T. M.; Moore, K.
898 A.; Lee, C.; Novak, G. A.; Sultana, C. M.; Wang, X. F.; Bertram, T. H.;
899 Prather, K. A.; Cappa, C. D. Linking variations in sea spray aerosol
900 particle hygroscopicity to composition during two microcosm
901 experiments. *Atmos. Chem. Phys.* **2016**, *16*, 9003–9018.

902 (28) Gard, E.; Mayer, J. E.; Morrical, B. D.; Dienes, T.; Fergenson,
903 D. P.; Prather, K. A. Real-Time Analysis of Individual Atmospheric
904 Aerosol Particles: Design and Performance of a Portable ATOFMS.
905 *Anal. Chem.* **1997**, *69*, 4083–4091.

906 (29) Gaston, C. J.; Cahill, J. F.; Collins, D. B.; Suski, K. J.; Ge, J. Y.;
907 Barkley, A. E.; Prather, K. A. The Cloud Nucleating Properties and
908 Mixing State of Marine Aerosols Sampled along the Southern
909 California Coast. *Atmosphere* **2018**, *9*, 52.

910 (30) Lee, C.; Sultana, C. M.; Collins, D. B.; Santander, M. V.; Axson,
911 J. L.; Malfatti, F.; Cornwell, G. C.; Grandquist, J. R.; Deane, G. B.;
912 Stokes, M. D.; Azam, F.; Grassian, V. H.; Prather, K. A. Advancing
913 Model Systems for Fundamental Laboratory Studies of Sea Spray
914 Aerosol Using the Microbial Loop. *J. Phys. Chem. A* **2015**, *119*, 8860–
915 8870.

916 (31) Mitts, B. A.; Wang, X. F.; Lucero, D. D.; Beall, C. M.; Deane, G.
917 B.; DeMott, P. J.; Prather, K. A. Importance of Supermicron Ice
918 Nucleating Particles in Nascent Sea Spray. *Geophys. Res. Lett.* **2021**,
919 *48*, No. e2020GL089633.

920 (32) Patterson, J. P.; Collins, D. B.; Michaud, J. M.; Axson, J. L.;
921 Sultana, C. M.; Moser, T.; Dommer, A. C.; Conner, J.; Grassian, V.
922 H.; Stokes, M. D.; Deane, G. B.; Evans, J. E.; Burkart, M. D.; Prather,
923 K. A.; Gianneschi, N. C. Sea Spray Aerosol Structure and
924 Composition Using Cryogenic Transmission Electron Microscopy.
925 *ACS Cent. Sci.* **2016**, *2*, 40–47.

926 (33) Quinn, P. K.; Collins, D. B.; Grassian, V. H.; Prather, K. A.;
927 Bates, T. S. Chemistry and Related Properties of Freshly Emitted Sea
928 Spray Aerosol. *Chem. Rev.* **2015**, *115*, 4383–4399.

929 (34) Schill, S. R.; Collins, D. B.; Lee, C.; Morris, H. S.; Novak, G. A.;
930 Prather, K. A.; Quinn, P. K.; Sultana, C. M.; Tivanski, A. V.;
931 Zimmermann, K.; Cappa, C. D.; Bertram, T. H. The Impact of
932 Aerosol Particle Mixing State on the Hygroscopicity of Sea Spray
933 Aerosol. *ACS Cent. Sci.* **2015**, *1*, 132–141.

934 (35) Tsigaridis, K.; Koch, D.; Menon, S. Uncertainties and
935 importance of sea spray composition on aerosol direct and indirect
936 effects. *J. Geophys. Res. Atmos.* **2013**, *118*, 220–235.

937 (36) Lim, C. Y.; Browne, E. C.; Sugrue, R. A.; Kroll, J. H. Rapid
938 heterogeneous oxidation of organic coatings on submicron aerosols. *Geophys. Res. Lett.* **2017**, *44*, 2949–2957.

939 (37) Lim, Y. B.; Ziemann, P. J. Chemistry of Secondary Organic
940 Aerosol Formation from OH Radical-Initiated Reactions of Linear,
941 Branched, and Cyclic Alkanes in the Presence of NO_x. *Aerosol. Sci. Technol.* **2009**, *43*, 604–619.

942 (38) Lim, Y. B.; Ziemann, P. J. Products and mechanism of
944 secondary organic aerosol formation from reactions of n-alkanes with
945 OH radicals in the presence of NO_x. *Environ. Sci. Technol.* **2005**, *39*, 946
9229–9236.

947 (39) Marshall, F. H.; Berkemeier, T.; Shiraiwa, M.; Nandy, L.; Ohm,
948 P. B.; Dutcher, C. S.; Reid, J. P. Influence of particle viscosity on mass
949 transfer and heterogeneous ozonolysis kinetics in aqueous-sucrose-
950 maleic acid aerosol. *Phys. Chem. Chem. Phys.* **2018**, *20*, 15560–15573.

951 (40) Shiraiwa, M.; Li, Y.; Tsimpidi, A. P.; Karydis, V. A.; Berkemeier,
952 T.; Pandis, S. N.; Lelieveld, J.; Koop, T.; Pöschl, U. Global
953 distribution of particle phase state in atmospheric secondary organic
954 aerosols. *Nat. Commun.* **2017**, *8*, 15002.

955 (41) Shiraiwa, M.; Zuend, A.; Bertram, A. K.; Seinfeld, J. H. Gas-
956 particle partitioning of atmospheric aerosols: interplay of physical
957 state, non-ideal mixing and morphology. *Phys. Chem. Chem. Phys.* **2013**, *15*,
958 11441–11453.

959 (42) Slade, J. H.; Knopf, D. A. Multiphase OH oxidation kinetics of
960 organic aerosol: The role of particle phase state and relative humidity.
961 *Geophys. Res. Lett.* **2014**, *41*, 5297–5306.

962 (43) Slade, J. H.; Shiraiwa, M.; Arangio, A.; Su, H.; Pöschl, U.;
963 Wang, J.; Knopf, D. A. Cloud droplet activation through oxidation of
964 organic aerosol influenced by temperature and particle phase state.
965 *Geophys. Res. Lett.* **2017**, *44*, 1583–1591.

966 (44) Slade, J. H.; Thalman, R.; Wang, J.; Knopf, D. A. Chemical
967 aging of single and multicomponent biomass burning aerosol
968 surrogate particles by OH: implications for cloud condensation
969 nucleus activity. *Atmos. Chem. Phys.* **2015**, *15*, 10183–10201.

970 (45) Trueblood, J. V.; Wang, X.; Or, V. W.; Alves, M. R.; Santander,
971 M. V.; Prather, K. A.; Grassian, V. H. The Old and the New: Aging of
972 Sea Spray Aerosol and Formation of Secondary Marine Aerosol
973 through OH Oxidation Reactions. *ACS Earth Space Chem.* **2019**, *3*,
974 2307–2314.

975 (46) George, I. J.; Abbott, J. P. D. Heterogeneous oxidation of
976 atmospheric aerosol particles by gas-phase radicals. *Nat. Chem.* **2010**,
977 *2*, 713–722.

978 (47) Kroll, J. H.; Lim, C. Y.; Kessler, S. H.; Wilson, K. R.
979 Heterogeneous Oxidation of Atmospheric Organic Aerosol: Kinetics
980 of Changes to the Amount and Oxidation State of Particle-Phase
981 Organic Carbon. *J. Phys. Chem. A* **2015**, *119*, 10767–10783.

982 (48) Kroll, J. H.; Smith, J. D.; Che, D. L.; Kessler, S. H.; Worsnop,
983 D. R.; Wilson, K. R. Measurement of fragmentation and
984 functionalization pathways in the heterogeneous oxidation of oxidized
985 organic aerosol. *Phys. Chem. Chem. Phys.* **2009**, *11*, 8005–8014.

986 (49) George, I. J.; Chang, R. Y. W.; Danov, V.; Vlasenko, A.; Abbatt,
987 J. P. D. Modification of cloud condensation nucleus activity of organic
988 aerosols by hydroxyl radical heterogeneous oxidation. *Atmos. Environ.* **2009**,
989 *43*, 5038–5045.

990 (50) Rosati, B.; Christiansen, S.; Dinesen, A.; Roldin, P.; Massling,
991 A.; Nilsson, E. D.; Bilde, M. The impact of atmospheric oxidation on
992 hygroscopicity and cloud droplet activation of inorganic sea spray
993 aerosol. *Sci. Rep.* **2021**, *11*, 10008.

994 (51) Kroll, J. H.; Donahue, N. M.; Jimenez, J. L.; Kessler, S. H.;
995 Canagaratna, M. R.; Wilson, K. R.; Altieri, K. E.; Mazzoleni, L. R.;
996 Wozniak, A. S.; Bluhm, H.; Mysak, E. R.; Smith, J. D.; Kolb, C. E.;
997 Worsnop, D. R. Carbon oxidation state as a metric for describing the
998 chemistry of atmospheric organic aerosol. *Nat. Chem.* **2011**, *3*, 133–
999 139.

1000 (52) Molina, M. J.; Ivanov, A. V.; Trakhtenberg, S.; Molina, L. T.
1001 Atmospheric evolution of organic aerosol. *Geophys. Res. Lett.* **2004**, *31*,
1002 L22104.

1003 (53) Cappa, C. D.; Che, D. L.; Kessler, S. H.; Kroll, J. H.; Wilson, K.
1004 R. Variations in organic aerosol optical and hygroscopic properties
1005

1006 upon heterogeneous OH oxidation. *J. Geophys. Res. Atmos.* **2011**, *116*,
1007 D15204.

1008 (54) Harmon, C. W.; Ruehl, C. R.; Cappa, C. D.; Wilson, K. R. A
1009 statistical description of the evolution of cloud condensation nuclei
1010 activity during the heterogeneous oxidation of squalane and bis(2-
1011 ethylhexyl) sebacate aerosol by hydroxyl radicals. *Phys. Chem. Chem.*
1012 *Phys.* **2013**, *15*, 9679–9693.

1013 (55) Lee, H. D.; Ray, K. K.; Tivanski, A. V. Solid, Semisolid, and
1014 Liquid Phase States of Individual Submicrometer Particles Directly
1015 Probed Using Atomic Force Microscopy. *Anal. Chem.* **2017**, *89*,
1016 12720–12726.

1017 (56) Murray, B. J. Inhibition of ice crystallisation in highly viscous
1018 aqueous organic acid droplets. *Atmos. Chem. Phys.* **2008**, *8*, 5423–
1019 5433.

1020 (57) Ray, K. K.; Lee, H. D.; Gutierrez, M. A.; Chang, F. J.; Tivanski,
1021 A. V. Correlating 3D Morphology, Phase State, and Viscoelastic
1022 Properties of Individual Substrate-Deposited Particles. *Anal. Chem.*
1023 **2019**, *91*, 7621–7630.

1024 (58) Knopf, D. A.; Alpert, P. A.; Wang, B. The Role of Organic
1025 Aerosol in Atmospheric Ice Nucleation: A Review. *ACS Earth Space
1026 Chem.* **2018**, *2*, 168–202.

1027 (59) Kang, E.; Root, M. J.; Toohey, D. W.; Brune, W. H.
1028 Introducing the concept of Potential Aerosol Mass (PAM). *Atmos.
1029 Chem. Phys.* **2007**, *7*, 5727–5744.

1030 (60) Lambe, A. T.; Ahern, A. T.; Williams, L. R.; Slowik, J. G.;
1031 Wong, J. P. S.; Abbatt, J. P. D.; Brune, W. H.; Ng, N. L.; Wright, J. P.;
1032 Croasdale, D. R.; Worsnop, D. R.; Davidovits, P.; Onasch, T. B.
1033 Characterization of aerosol photooxidation flow reactors: heteroge-
1034 neous oxidation, secondary organic aerosol formation and cloud
1035 condensation nuclei activity measurements. *Atmos. Meas. Tech.* **2011**,
1036 *4*, 445–461.

1037 (61) Lee, H. D.; Kaluarachchi, C. P.; Hasenecz, E. S.; Zhu, J. Z.;
1038 Popa, E.; Stone, E. A.; Tivanski, A. V. Effect of dry or wet substrate
1039 deposition on the organic volume fraction of core-shell aerosol
1040 particles. *Atmos. Meas. Tech.* **2019**, *12*, 2033–2042.

1041 (62) Ryder, O. S.; Campbell, N. R.; Morris, H.; Forestieri, S.;
1042 Ruppel, M. J.; Cappa, C.; Tivanski, A.; Prather, K.; Bertram, T. H.
1043 Role of Organic Coatings in Regulating N₂O₅ Reactive Uptake to Sea
1044 Spray Aerosol. *J. Phys. Chem. A* **2015**, *119*, 11683–11692.

1045 (63) Cappa, C. D.; Asadi, S.; Barreda, S.; Wexler, A. S.; Bouvier, N.
1046 M.; Ristenpart, W. D. Expiratory aerosol particle escape from surgical
1047 masks due to imperfect sealing. *Sci. Rep.* **2021**, *11*, 12110.

1048 (64) Cappa, C.; Ristenpart, W. D.; Barreda, S.; Bouvier, N. M.;
1049 Levintal, E.; Wexler, A. S.; Roman, S. A. A highly efficient cloth
1050 facemask design. *Aerosol Sci. Technol.* **2022**, *56*, 12–28.

1051 (65) Gupta, A.; Rawlings, J. B. Comparison of parameter estimation
1052 methods in stochastic chemical kinetic models: Examples in systems
1053 biology. *AIChE J.* **2014**, *60*, 1253–1268.

1054 (66) Laskina, O.; Morris, H. S.; Grandquist, J. R.; Qin, Z.; Stone, E.
1055 A.; Tivanski, A. V.; Grassian, V. H. Size Matters in the Water Uptake
1056 and Hygroscopic Growth of Atmospherically Relevant Multi-
1057 component Aerosol Particles. *J. Phys. Chem. A* **2015**, *119*, 4489–4497.

1058 (67) Morris, H. S.; Estillore, A. D.; Laskina, O.; Grassian, V. H.;
1059 Tivanski, A. V. Quantifying the Hygroscopic Growth of Individual
1060 Submicrometer Particles with Atomic Force Microscopy. *Anal. Chem.*
1061 **2016**, *88*, 3647–3654.

1062 (68) Estillore, A. D.; Morris, H. S.; Or, V. W.; Lee, H. D.; Alves, M.
1063 R.; Marciano, M. A.; Laskina, O.; Qin, Z.; Tivanski, A. V.; Grassian, V.
1064 H. Linking hygroscopicity and the surface microstructure of model
1065 inorganic salts, simple and complex carbohydrates, and authentic sea
1066 spray aerosol particles. *Phys. Chem. Chem. Phys.* **2017**, *19*, 21101–
1067 21111.

1068 (69) Jayarathne, T.; Stockwell, C. E.; Yokelson, R. J.; Nakao, S.;
1069 Stone, E. A. Emissions of Fine Particle Fluoride from Biomass
1070 Burning. *Environ. Sci. Technol.* **2014**, *48*, 12636–12644.

1071 (70) Schauer, J. J.; Mader, B. T.; DeMinter, J. T.; Heidemann, G.;
1072 Bae, M. S.; Seinfeld, J. H.; Flagan, R. C.; Cary, R. A.; Smith, D.;
1073 Huebert, B. J.; Bertram, T.; Howell, S.; Kline, J. T.; Quinn, P.; Bates,
1074 T.; Turpin, B.; Lim, H. J.; Yu, J. Z.; Yang, H.; Keywood, M. D. ACE-

1075 Asia intercomparison of a thermal-optical method for the determi-
1076 nation of particle-phase organic and elemental carbon. *Environ. Sci. 1076
Technol.* **2003**, *37*, 993–1001.

1077 (71) Holland, H. D. *The Chemistry of the Atmosphere and Oceans*;
1078 Wiley: New York, 1978.

1079 (72) Chim, M. M.; Cheng, C. T.; Davies, J. F.; Berkemeier, T.;
1080 Shiraiwa, M.; Zuend, A.; Chan, M. N. Compositional evolution of
1081 particle-phase reaction products and water in the heterogeneous OH
1082 oxidation of model aqueous organic aerosols. *Atmos. Chem. Phys.*
1083 **2017**, *17*, 14415–14431.

1084 (73) Marshall, F. H.; Miles, R. E. H.; Song, Y.-C.; Ohm, P. B.;
1085 Power, R. M.; Reid, J. P.; Dutcher, C. S. Diffusion and reactivity in
1086 ultraviscous aerosol and the correlation with particle viscosity. *Chem.
1087 Sci.* **2016**, *7*, 1298–1308.

1088 (74) McNeill, V. F.; Yatavelli, R. L. N.; Thornton, J. A.; Stipe, C. B.;
1089 Landgrebe, O. Heterogeneous OH oxidation of palmitic acid in single
1090 component and internally mixed aerosol particles: vaporization and
1091 the role of particle phase. *Atmos. Chem. Phys.* **2008**, *8*, 5465–5476.

1092 (75) Athanasiadis, A.; Fitzgerald, C.; Davidson, N. M.; Giorio, C.;
1093 Botchway, S. W.; Ward, A. D.; Kalberer, M.; Pope, F. D.; Kuimova, M.
1094 K. Dynamic viscosity mapping of the oxidation of squalene aerosol
1095 particles. *Phys. Chem. Chem. Phys.* **2016**, *18*, 30385–30393.

1096 (76) Saukko, E.; Lambe, A. T.; Massoli, P.; Koop, T.; Wright, J. P.;
1097 Croasdale, D. R.; Pedernera, D. A.; Onasch, T. B.; Laaksonen, A.;
1098 Davidovits, P.; Worsnop, D. R.; Virtanen, A. Humidity-dependent
1099 phase state of SOA particles from biogenic and anthropogenic
1100 precursors. *Atmos. Chem. Phys.* **2012**, *12*, 7517–7529.

1101 (77) Rinaldi, M.; De Cesari, S.; Finessi, E.; Giulianelli, L.; Carbone,
1102 C.; Fuzzi, S.; O'Dowd, C. D.; Ceburnis, D.; Facchini, M. C. Primary
1103 and Secondary Organic Marine Aerosol and Oceanic Biological
1104 Activity: Recent Results and New Perspectives for Future Studies.
1105 *Adv. Meteorol.* **2010**, *2010*, 310682.

1106 (78) Maria, S. F.; Russell, L. M.; Turpin, B. J.; Porcja, R. J. FTIR
1107 measurements of functional groups and organic mass in aerosol
1108 samples over the Caribbean. *Atmos. Environ.* **2002**, *36*, 5185–5196.

1109 (79) Or, V. W.; Estillore, A. D.; Tivanski, A. V.; Grassian, V. H. Lab
1110 on a tip: atomic force microscopy - photothermal infrared
1111 spectroscopy of atmospherically relevant organic/inorganic aerosol
1112 particles in the nanometer to micrometer size range. *Analyst* **2018**,
1113 *143*, 2765–2774.

1114 (80) Nakamoto, K. Applications in Inorganic Chemistry. *Infrared
1115 and Raman Spectra of Inorganic and Coordination Compounds*; Wiley,
1116 2008; pp 149–354.

1117 (81) Parikh, S. J.; Chorover, J. Infrared spectroscopy studies of
1118 cation effects on lipopolysaccharides in aqueous solution. *Colloids
1119 Surf. B* **2007**, *55*, 241–250.

1120 (82) Wiercigroch, E.; Szafraniec, E.; Czamara, K.; Pacia, M. Z.;
1121 Majzner, K.; Kochan, K.; Kaczor, A.; Baranska, M.; Malek, K. Raman
1122 and infrared spectroscopy of carbohydrates: A review. *Spectrochim.
1123 Acta, Part A* **2017**, *185*, 317–335.

1124 (83) Papageorgiou, S. K.; Kouvelos, E. P.; Favvas, E. P.; Sapalidis, A.
1125 A.; Romanos, G. E.; Katsaros, F. K. Metal–carboxylate interactions in
1126 metal–alginate complexes studied with FTIR spectroscopy. *Carbo-
1127 hydr. Res.* **2010**, *345*, 469–473.

1128 (84) Morris, H. S.; Grassian, V. H.; Tivanski, A. V. Correction:
1129 Humidity-dependent surface tension measurements of individual
1130 inorganic and organic submicrometre liquid particles. *Chem. Sci.* **2015**,
1131 *6*, 6021.

1132 (85) Kuwata, M.; Martin, S. T. Phase of atmospheric secondary
1133 organic material affects its reactivity. *Proc. Natl. Acad. Sci. U.S.A.* **2012**,
1134 *109*, 17354–17359.

1135 (86) Kuwata, M.; Martin, S. T. Particle Size Distributions following
1136 Condensational Growth in Continuous Flow Aerosol Reactors as
1137 Derived from Residence Time Distributions: Theoretical Develop-
1138 ment and Application to Secondary Organic Aerosol. *Aerosol. Sci.
1139 Technol.* **2012**, *46*, 937–949.

1140 (87) Ault, A. P.; Axson, J. L. Atmospheric Aerosol Chemistry:
1141 Spectroscopic and Microscopic Advances. *Anal. Chem.* **2017**, *89*,
1142 430–452.

1143

1144 (88) Riemer, N.; Ault, A. P.; West, M.; Craig, R. L.; Curtis, J. H.
1145 Aerosol Mixing State: Measurements, Modeling, and Impacts. *Rev.*
1146 *Geophys.* **2019**, *57*, 187–249.

1147 (89) Shiraiwa, M.; Ammann, M.; Koop, T.; Pöschl, U. Gas uptake
1148 and chemical aging of semisolid organic aerosol particles. *Proc. Natl.*
1149 *Acad. Sci. U.S.A.* **2011**, *108*, 11003–11008.

1150 (90) Carslaw, K. S.; Lee, L. A.; Reddington, C. L.; Pringle, K. J.; Rap,
1151 A.; Forster, P. M.; Mann, G. W.; Spracklen, D. V.; Woodhouse, M. T.;
1152 Regayre, L. A.; Pierce, J. R. Large contribution of natural aerosols to
1153 uncertainty in indirect forcing. *Nature* **2013**, *503*, 67–71.

1154 (91) Pajunoja, A.; Hu, W.; Leong, Y. J.; Taylor, N. F.; Miettinen, P.;
1155 Palm, B. B.; Mikkonen, S.; Collins, D. R.; Jimenez, J. L.; Virtanen, A.
1156 Phase state of ambient aerosol linked with water uptake and chemical
1157 aging in the southeastern US. *Atmos. Chem. Phys.* **2016**, *16*, 11163–
1158 11176.

1159 (92) Facchini, M. C.; Rinaldi, M.; Decesari, S.; Carbone, C.; Finessi,
1160 E.; Mircea, M.; Fuzzi, S.; Ceburnis, D.; Flanagan, R.; Nilsson, E. D.;
1161 de Leeuw, G.; Martino, M.; Woeltjen, J.; O'Dowd, C. D. Primary
1162 submicron marine aerosol dominated by insoluble organic colloids
1163 and aggregates. *Geophys. Res. Lett.* **2008**, *35*, L17814.

1164 (93) Murray, B. J.; Wilson, T. W.; Dobbie, S.; Cui, Z. Q.; Al-Jumur,
1165 S. M. R. K.; Möhler, O.; Schnaiter, M.; Wagner, R.; Benz, S.;
1166 Niemand, M.; Saathoff, H.; Ebert, V.; Wagner, S.; Kärcher, B.
1167 Heterogeneous nucleation of ice particles on glassy aerosols under
1168 cirrus conditions. *Nat. Geosci.* **2010**, *3*, 233–237.

1169 (94) Berkemeier, T.; Steimer, S. S.; Krieger, U. K.; Peter, T.; Pöschl,
1170 U.; Ammann, M.; Shiraiwa, M. Ozone uptake on glassy, semi-solid
1171 and liquid organic matter and the role of reactive oxygen
1172 intermediates in atmospheric aerosol chemistry. *Phys. Chem. Chem.*
1173 *Phys.* **2016**, *18*, 12662–12674.

1174 (95) Koop, T.; Bookhold, J.; Shiraiwa, M.; Pöschl, U. Glass
1175 transition and phase state of organic compounds: dependency on
1176 molecular properties and implications for secondary organic aerosols
1177 in the atmosphere. *Phys. Chem. Chem. Phys.* **2011**, *13*, 19238–19255.

1178 (96) Virtanen, A.; Joutsensaari, J.; Koop, T.; Kannisto, J.; Yli-Pirilä,
1179 P.; Leskinen, J.; Mäkelä, J. M.; Holopainen, J. K.; Pöschl, U.; Kulmala,
1180 M.; Worsnop, D. R.; Laaksonen, A. An amorphous solid state of
1181 biogenic secondary organic aerosol particles. *Nature* **2010**, *467*, 824–
1182 827.